nature catalysis

Article

https://doi.org/10.1038/s41929-023-01005-3

Strain enhances the activity of molecular electrocatalysts via carbon nanotube supports

Received: 24 December 2022

Accepted: 13 July 2023

Published online: 14 August 2023

Check for updates

Jianjun Su[1,9], Charles B. Musgrave III[2,9], Yun Song[1], Libei Huang[1], Yong Liu[1], Geng Li[1], Yinger Xin[1], Pei Xiong[3], Molly Meng-Jung Li[3], Haoran Wu[4], Minghui Zhu[4], Hao Ming Chen[5], Jianyu Zhang[6], Hanchen Shen[6], Ben Zhong Tang[6], Marc Robert[7], William A. Goddard III[2] ✉ & Ruquan Ye[1,8] ✉

Support-induced strain engineering is useful for modulating the properties of two-dimensional materials. However, controlling strain of planar molecules is technically challenging due to their sub-2 nm lateral size. Additionally, the effect of strain on molecular properties remains poorly understood. Here we show that carbon nanotubes (CNTs) are ideal substrates for inducing optimum properties through molecular curvature. In a tandem-flow electrolyser with monodispersed cobalt phthalocyanine (CoPc) on single-walled CNTs (CoPc/SWCNTs) for CO_2 reduction, we achieve a methanol partial current density of >90 mA cm^{-2} with >60% selectivity, surpassing wide multiwalled CNTs at 16.6%. We report vibronic and X-ray spectroscopies to unravel the distinct local geometries and electronic structures induced by the strong molecule–support interactions. Grand canonical density functional theory confirms that curved CoPc/SWCNTs improve *CO binding to enable subsequent reduction, whereas wide multiwalled CNTs favour CO desorption. Our results show the important role of SWCNTs beyond catalyst dispersion and electron conduction.

The use of curved supports to induce local strain is well established for modulating properties of conventional layered materials[1]. An excellent example is graphene, which already exhibits remarkable properties in its planar configuration. Straining graphene can modify its electronic structure to create polarized carrier puddles, induce pseudomagnetic fields and alter surface properties[2]. In MoS_2, modifying the supporting glass sphere diameter induces curvature in the MoS_2, which permits precise bandgap tuning of MoS_2 in a continuous range up to as high as 360 meV (ref. 3). Curved MoS_2 conformally coated on gold nanocone arrays is a promising catalyst for the hydrogen evolution reaction (HER). The improved HER activity is attributed to sulfur vacancies and reduction of the bandgap under strain[4]. Graphene and MoS_2 are good candidates for strain engineering because they are relatively large (millimetre) in size. However, strain induction for sub-2 nm materials

[1]Department of Chemistry, State Key Laboratory of Marine Pollution, City University of Hong Kong, Hong Kong, China. [2]Materials and Process Simulation Center, California Institute of Technology, Pasadena, CA, USA. [3]Department of Applied Physics, Hong Kong Polytechnic University, Hong Kong, China. [4]State Key Laboratory of Chemical Engineering, East China University of Science and Technology, Shanghai, China. [5]Department of Chemistry, National Taiwan University, Taipei, Taiwan. [6]School of Science and Engineering, Shenzhen Institute of Aggregate Science and Technology, The Chinese University of Hong Kong, Shenzhen (CUHK-Shenzhen), Shenzhen, China. [7]Université Paris Cité, Laboratoire d'Electrochimie Moléculaire, CNRS, Paris, France. [8]City University of Hong Kong Shenzhen Research Institute, Shenzhen, China. [9]These authors contributed equally: Jianjun Su, Charles B. Musgrave III. ✉e-mail: wag@caltech.edu; ruquanye@cityu.edu.hk

is challenging due to the mismatch of lateral size with supports and difficulties in material transfer.

Molecular complexes such as metalloporphyrins and metallophthalocyanines are efficient CO_2 reduction reaction (CO_2RR) catalysts because of their electronic structures and the tunable ligand environments surrounding the active sites[5]. However, these molecules, along with most other molecular catalysts, primarily reduce CO_2 to CO; molecular catalysts that selectively reduce CO_2 beyond CO are scarcely reported[6,7]. An early study of cobalt phthalocyanine (CoPc) in 1984[8] showed a methanol Faradaic efficiency (FE) of <5%. This work did not receive much attention until recently, when the Wang[9,10] and Robert[11] groups separately reported improved FE_{MeOH} with CoPc deposited on multiwalled carbon nanotubes (MWCNTs). The Wang group found that a FE_{MeOH} as high as 44% could be obtained with highly dispersed CoPc on MWCNTs. Independently, the Robert group reported a different method for preparing CoPc–MWCNT composite, which only generated a small amount of methanol from CO_2RR, but a larger amount from the CO reduction reaction (CORR). To date, most CoPc-based catalysts produce CO as the prevailing product without generating substantial methanol[12–16]. Therefore, it remains challenging to realize and understand the ability of CoPc to catalyse the CO_2RR beyond the prominent CO product.

CNTs are exceptional support materials for heterogeneous catalysis. Their large specific surface areas readily disperse nanoparticles, avoiding agglomeration, and their high electronic conductivities make them promising for electrochemical applications. Here we present insights into the role of CNTs in heterogeneous electrocatalysis. Due to recent advancements in synthesis and purification, the diameters of CNTs can be controlled from 2 nm to >50 nm, making them ideal supports for inducing strain in sub-2 nm planar molecules. We report X-ray spectroscopic studies and other spectra to assess the structure of molecular CoPc before and after monodispersion on various CNTs. We observe substantial molecular distortion and strong molecule–CNT interactions for SWCNTs. This is supported by our density functional theory (DFT) calculations. We find that increased molecular curvature strengthens *CO absorption, which enables further reduction towards methanol, whereas flat CoPc favours CO desorption, thus forming CO as the main product. As a result, the distorted CoPc/single-walled carbon nanotubes (SWCNTs) exhibit a 385% improvement in FE_{MeOH} compared to CoPc/MWCNTs. We also extend these findings to oxygen reduction reaction (ORR) and CO_2RR studies on SWCNTs, which also exhibit strain-dependent catalytic activity.

Results

Materials synthesis and characterization

Metallophthalocyanines deposited on different CNTs are denoted as MPc/X, where M is the metal and X refers to SWCNTs or the average diameter (in nm) of the MWCNTs (Supplementary Figs. 1 and 2). Depending on the local interactions between curved CNTs and the overlayer, molecules may undergo controllable distortion to alleviate strain (Fig. 1a). Assuming the overlayer is fully elastic and the interlayer distance is 0.3 nm, the bending angle can range from ~96° (for 1-nm-diameter CNTs) to ~1.5° (for 100-nm-diameter CNTs) (see Supplementary Note 1 for estimates). Scanning transmission electron microscopy energy-dispersive X-ray spectroscopy (STEM-EDS) mapping shows a uniform distribution of N and Co along the SWCNT surface (Fig. 1b–e). In aberration-corrected high-angle annular dark-field (HAADF)-STEM (Fig. 1f), the bright spots marked with red circles further verify the uniformly dispersed cobalt sites.

We sought to elucidate how interactions of CoPc with CNTs might affect catalysis. Early studies suggested that deformed phthalocyanines will have varied vibronic and electronic structures[17,18]. We first characterized the Raman spectra for CoPc and various bare and CoPc-decorated CNTs (Supplementary Figs. 3 and 4)[19]. In comparison, CoPc/SWCNTs show a prominent peak at 250–290 cm^{-1}, assigned to the Co–N out-of-plane deformation and ring boating[20]. This enhanced out-of-plane signal has been frequently observed on strained/curved two-dimensional materials[3,21]. Interaction with the CNTs involving π–π stacking and through-space orbital coupling could lead to additional charge-transfer processes[22]. This is validated by the ultraviolet–visible spectra of the catalysts, showing a redshift at the Q band of the CoPc molecules after deposition on CNTs (Supplementary Fig. 5)[23,24]. X-ray photoelectron spectroscopy (XPS) shows that both the Co $2p_{1/2}$ and Co $2p_{3/2}$ peaks of CoPc/CNTs shift to higher binding energies (Fig. 2a), reaching a maximum difference of 1.2 eV for CoPc/SWCNTs. The signal evolution is even more prominent for the N 1*s* peak (Fig. 2b). Previous reports have studied the interactions of MPc with various substrates such as TiO_2, gold and other semiconductors[25,26]. It was thought that the strong molecule–substrate interaction would induce a peak splitting, while a weak interaction would cause only a peak shift. Indeed, we observe a new peak at >400 eV for all the CoPc/CNT samples. CoPc/SWCNTs show the most intense new peak at ~400.5 eV, implying strong CoPc–SWCNT interactions. The peak splitting of CoPc/SWCNTs is ~1.3 eV, attributed to the shifted N 1*s* energies according to the theoretical calculations discussed below. The $E_{1/2}(Co^{I}/Co^{II})$ redox potential also shifts from 0.162 V for CoPc/50 to 0.119 V for CoPc/SWCNTs (Supplementary Fig. 6), which is similar to the deformed ZnPc attributed to the destabilization of the highest occupied molecular orbital[18]. The above experimental data suggest distinct molecular structures exist on different CNT supports.

To understand the local structures of the CoPc/CNTs, we performed X-ray absorption near-edge structure (XANES) and extended X-ray absorption fine structure (EXAFS) analyses of cobalt. As shown in Fig. 2c, the Co K-edge XANES spectrum exhibits an obvious peak at 7,715 eV; this $1s \rightarrow 4p_z$ transition is indicative of the $Co–N_4$ structure[27]. A decline in the $1s \rightarrow 4p_z$ transition is observed when CNTs are introduced, probably due to the decreased symmetry (D_{4h} to C_{4v}). The peaks near 7,725 eV result from the $1s \rightarrow 4p_{x,y}$ transition, with the exact peak position dependent on the valency of cobalt[28]. The peak position of CoPc/CNTs shifts slightly to lower energy compared to CoPc, indicating charge transfer between CoPc and the CNTs. The Fourier transform of the EXAFS spectra shows the coordination environment around the cobalt sites (Fig. 2d and Supplementary Fig. 7). The signal can be catalogued into three groups: [CoPc, CoPc/50], [CoPc/25, CoPc/15] and [CoPc/5, CoPc/SWCNT]. As the CNT diameter decreases, both the Co–N1 (first coordination sphere) and Co–C1 (second coordination sphere) distances increase. The Co–N1 and Co–C1 peak deviations indicate distortion of the CoPc molecule[29]. In addition, the peak intensities increase with smaller-diameter CNTs; this increased cobalt coordination number is a result of stronger interaction of CoPc with the CNTs, as inferred from signal fitting. The fitted EXAFS signals (Fig. 2e,f, Supplementary Figs. 8 and 9, and Supplementary Table 1) imply molecular bending around the CNTs. The high degree of molecular bending for CoPc/SWCNTs leads to elongated Co–N1 and Co–C1 distances (Supplementary Table 1). In addition, the intensity of the Co–C1 peak increases due to strong $Co–C_{SWCNT}$ interactions. For CoPc/50, the local CNT curvature is negligible, such that CoPc remains planar. Consequently, the CoPc/50 coordination environment is similar to that of the pristine CoPc molecule. Because the EXAFS only gives information about the coordination environment around the cobalt centre, an expanded flat CoPc with longer Co–N1 and Co–C1 bonds would also be a possible structure. However, our molecular dynamics (MD) calculations, discussed in the computation part later, suggest such configuration is unfavourable. In addition, the flat configuration cannot explain the experimental Raman, $E_{1/2}(Co^{I}/Co^{II})$ and XPS data and the electrochemical performance.

Electrochemical CO_2 reduction performance of CoPc/SWCNTs

The electrochemical CO_2RR was carried out in a custom glass H-cell with 0.5 M $KHCO_3$. The number of electrochemically active cobalt sites is

https://doi.org/10.1038/s41929-023-01005-3

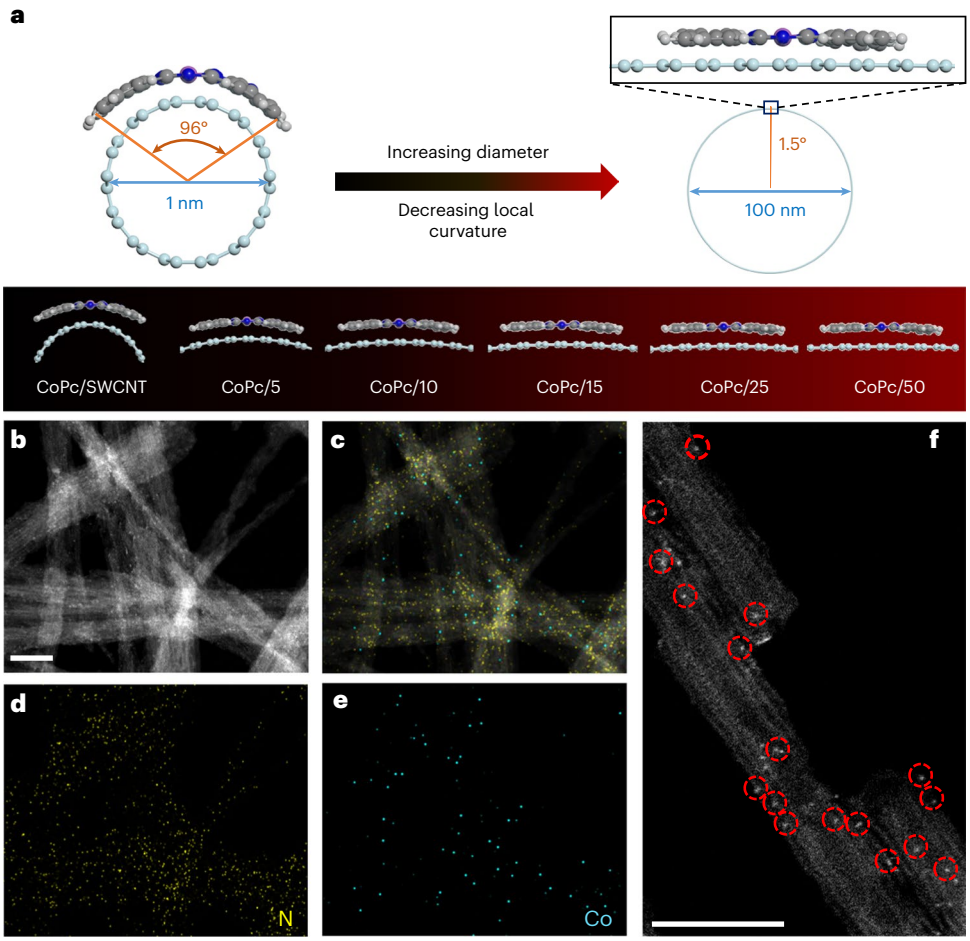

Fig. 1 | Morphologies of CoPc on different CNTs. a, Illustration of the structural distortion of CoPc on different-diameter CNTs, assuming CoPc is fully elastic. **b**–**e**, HAADF-STEM (**b**) and EDS elemental mapping for overlap (**c**) N (**d**) and Co (**e**) of CoPc/SWCNTs. **f**, Aberration-corrected HAADF-STEM of CoPc/SWCNTs showing isolated cobalt atoms (red circles) on the SWCNT surface. Scale bars: **b**, 20 nm; **f**, 5 nm.

similar among the different samples as indicated by the anodic Co^{I}/Co^{II} peak areas (Supplementary Fig. 6). Supplementary Fig. 10 shows the cyclic voltammograms (CVs) for CoPc/SWCNT, CoPc/15 and CoPc/50 catalysts in CO_2-saturated solution. The currents are very pronounced relative to the bare SWCNT, MWCNT/15 and MWCNT/50 supports. The CO_2RR selectivities of CoPc/SWCNTs, CoPc/15 and CoPc/50 were further evaluated at various potentials via chronoamperometry tests (Supplementary Fig. 11). NMR and gas chromatography (GC) measurements were made to analyse the liquid and gas products, respectively. As shown in Fig. 3a, FE_{MeOH} exhibits the typical volcano-like dependence on applied potential from −0.78 to −1.03 V versus RHE. At −0.93 V, a maximum FE_{MeOH} of 53.4% is achieved for CoPc/SWCNTs, which is much higher than that of CoPc/15 (17.1% at −0.93 V) and CoPc/50 (13.9% at −0.93 V). A maximum methanol partial current density (j_{MeOH}) of 8.8 mA cm^{-2} is achieved at −0.93 V for CoPc/SWCNTs (Supplementary Fig. 12) compared to the 1.9 mA cm^{-2} for CoPc/15 and 1.5 mA cm^{-2} for CoPc/50. To confirm that methanol is derived from CO_2 rather than from other impurities, isotopic-labelling experiments were conducted in $^{13}CO_2$-saturated 0.5 M $KH^{13}CO_3$ under continuous $^{13}CO_2$ flow. The peak splitting of ^{1}H NMR at 3.32 ppm and the obvious ^{13}C NMR peak at 49.11 ppm verifies that the methanol produced originates from the CO_2 input[11,30] (Supplementary Fig. 13). The bare CoPc, SWCNT and MWCNT/15 samples show negligible electrocatalytic CO_2RR activity with little CO produced throughout the potential window (Supplementary Fig. 14). In the durability test, the CoPc/SWCNTs maintained ~30% FE_{MeOH} for 10 h at an operating total current density of 16 mA cm^{-2} (Supplementary Fig. 15). Supplementary Fig. 16 shows the relation of FE_{MeOH} with CoPc loading on SWCNTs. Increasing the CoPc:SWCNT ratio from 1:50 to 1:3 and 1:1 did not increase FE_{MeOH}. This could be explained by CoPc–CoPc stacking at high loadings that weakens the support effect. High CoPc loading also leads to catalyst leaching during chronoamperometry.

We next explored how FE_{MeOH} varies with CNT diameter at −0.93 V (Supplementary Fig. 17). The FE_{MeOH} decreases from 53.2% for CoPc/SWCNTs to 13.9% for CoPc/50. The conversion of CO_2 to methanol involves six electron transfers, so that high charge transfer resistance will negatively affect FE_{MeOH}. Electrochemical impedance spectroscopy (EIS) at −0.93 V shows that CoPc/SWCNTs have less charge transfer resistance than CoPc/15 and CoPc/50, indicating more facile substrate reduction with CoPc/SWCNTs (Supplementary Fig. 18).

To examine the role of the electronic structure of SWCNTs, we used metallic and semiconducting SWCNTs (SWCNT-M or SWCNT-S) as supports for catalyst preparation. SWCNT-M and SWCNT-S show distinct ultraviolet absorption at 600–800 nm and 900–1,100 nm for the M_{11} and S_{22} peaks, respectively (Supplementary Fig. 19). CoPc/SWCNT-M and SWCNT-S exhibit similar FE_{MeOH} and j_{MeOH} to those of CoPc/SWCNTs at −0.93 V (Supplementary Fig. 20d), suggesting that the SWCNT electronic structure does not play a major role in steering the multielectron reduction.

To highlight the necessity of the CoPc–SWCNT interfacial configuration, we covalently anchored CoPc to the surface of SWCNTs (Supplementary Fig. 20a), leading to a flat CoPc vertically bound to SWCNTs

https://doi.org/10.1038/s41929-023-01005-3

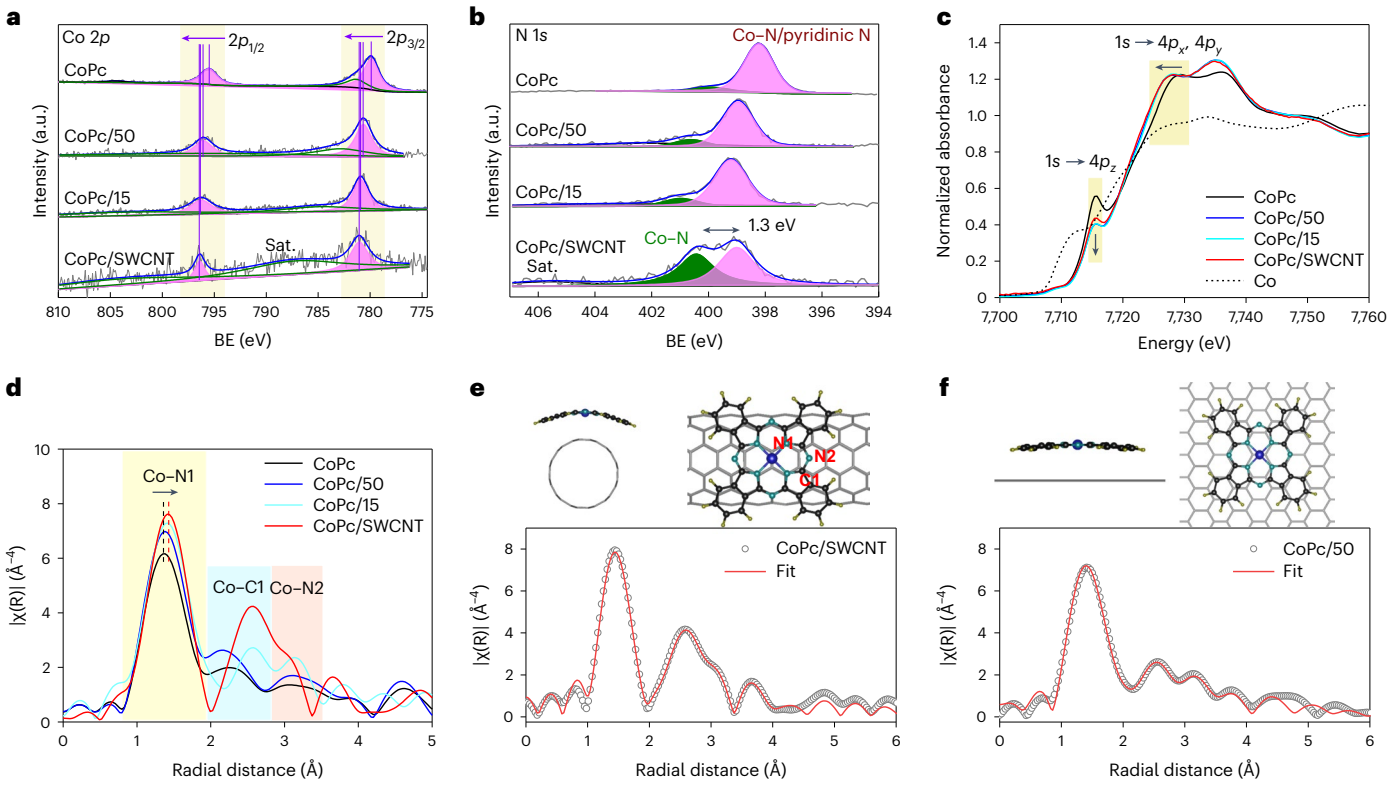

Fig. 2 | X-ray spectroscopic characterizations. a,**b**, XPS of Co 2*p* (**a**) and N 1*s* (**b**) for CoPc/SWCNTs, CoPc/15, CoPc/50 and CoPc. **c**, XANES Co K-edge spectrum. **d**, Fourier transform EXAFS. **e**,**f**, Simulated structures and EXAFS fitting in R space for curved CoPc/SWCNTs (**e**) and flat CoPc/50 (**f**). N1, N2, nitrogen atoms in the first and second coordination spheres.

(f-CoPc-SWCNTs). The N 1*s* XPS peak of f-CoPc-SWCNTs exhibits no peak splitting and the out-of-plane deformation signal does not emerge (Supplementary Fig. 20b,c); these features are distinct from CoPc/SWCNTs but similar to pristine CoPc. Moreover, the f-CoPc-SWCNTs only reach 15.5% FE_{MeOH} and a j_{MeOH} of 1.6 mA cm^{-2}, which is similar to the performance of CoPc/50 (Supplementary Fig. 20d).

High current density in CO_2RR and CORR using a flow cell

The CO_2RR current density is limited in the H-cell by low CO_2 solubility and mass transport in aqueous electrolyte. To achieve higher j_{MeOH}, we constructed a flow cell featuring a gas diffusion electrode (Supplementary Fig. 21a). In the flow cell, 0.1 M KOH + 3 M KCl (instead of $KHCO_3$) was used as the catholyte to improve j_{MeOH} and suppress the HER at high potential[11,31,32]. The total current density in the flow cell is substantially higher (Supplementary Fig. 21b) than that of the H-cell at all applied potentials. The maximum j_{MeOH} of CoPc/SWCNTs reaches 66.8 mA cm^{-2} with a 31.3% FE_{MeOH} at −0.9 V versus RHE, which is 7.6 times that of j_{MeOH} in the H-cell (Fig. 3b,c). The maximum j_{MeOH} of CoPc/15 and CoPc/50 are 21.7 mA cm^{-2} (15.6% FE_{MeOH}) and 9.3 mA cm^{-2} (9.3% FE_{MeOH}) at −0.9 V versus RHE, respectively. Additionally, CoPc/SWCNTs exhibit a stable total current density with no loss for 20 min at various potentials (Supplementary Fig. 22). Even at 200 mA cm^{-2} (−0.9 V versus RHE), the FE_{MeOH} is maintained at ~26% for 10 h without decay (Supplementary Figs. 23 and 24).

Because the electrochemical reduction of CO_2 to methanol is a multistep process with CO being the important intermediate[9], methanol production will be inhibited by *H and *CO_2 adsorption. Competition with *CO_2 adsorption can be resolved by a tandem reaction. Specifically, CO_2 can be first reduced to CO with >95% FE, and then the produced CO can be further reduced to methanol in a second electrolyser free of CO_2 in alkaline media. We conducted direct CO reduction in a flow cell identical to the parent CO_2RR process, except that CO was used as the feed gas to achieve higher FE_{MeOH} and j_{MeOH}. For CoPc/SWCNTs, j_{MeOH} reaches 62.1 mA cm^{-2} at −0.8 V_{RHE} with a corresponding FE_{MeOH} of 50.5% (Fig. 3d and Supplementary Fig. 25). This corresponds to a FE_{MeOH} of 60.1% for the tandem reaction, assuming a 95% FE_{CO} from CO_2 (Supplementary Note 2). CoPc/15 and CoPc/50 achieve j_{MeOH}s of only 20.5 mA cm^{-2} and 15.5 mA cm^{-2} with FE_{MeOH}s of 21.8% and 16.6%, respectively (Fig. 3e and Supplementary Fig. 26). Moreover, the CORR with CoPc/SWCNTs maintains a total current density of 100 mA cm^{-2} at an FE_{MeOH} of ~50% for 10 h (Fig. 3f and Supplementary Fig. 27).

An extremely high applied potential would overreduce the Pc ligand, resulting in deactivation via demetallation[9]. After the stability test, the Raman spectrum confirms the presence of the SWCNTs and the curved CoPc structure. The ultraviolet–visible absorption spectrum and X-ray diffraction patterns of CoPc/SWCNTs display no new peaks related to cobalt metal or cobalt oxide, indicating no demetallation (Supplementary Fig. 28).

Interface configuration predicted by theory

We find that binding the CoPc catalyst to the CNT walls changes the geometric and electronic structure. To further investigate this, we employed MD calculations using the universal force field (UFF)[33]. These MD simulations used the polarizable charge equilibration (PQEq)[34] scheme for electrostatics and the RexPoN universal non-bond (UNB)[35] van der Waals interactions (UFF is used solely for valence terms). Using UFF + PQEq + UNB allows us to obtain molecular geometries at the accuracy level of high-quality quantum mechanics while at the cost of classical mechanics. The ability of PQEq + UNB ability to accurately capture non-bond geometries has been proven previously for several crystal systems[35].

We estimate that the smallest SWCNTs in our experiments have a diameter of ~2 nm. To model the SWCNTs, we use a large $C_{116}H_{28}$ graphitic sheet which has a curvature matching that of a SWCNT with 2 nm diameter (Supplementary Figs. 29 and 30); the 116 carbon atoms

https://doi.org/10.1038/s41929-023-01005-3

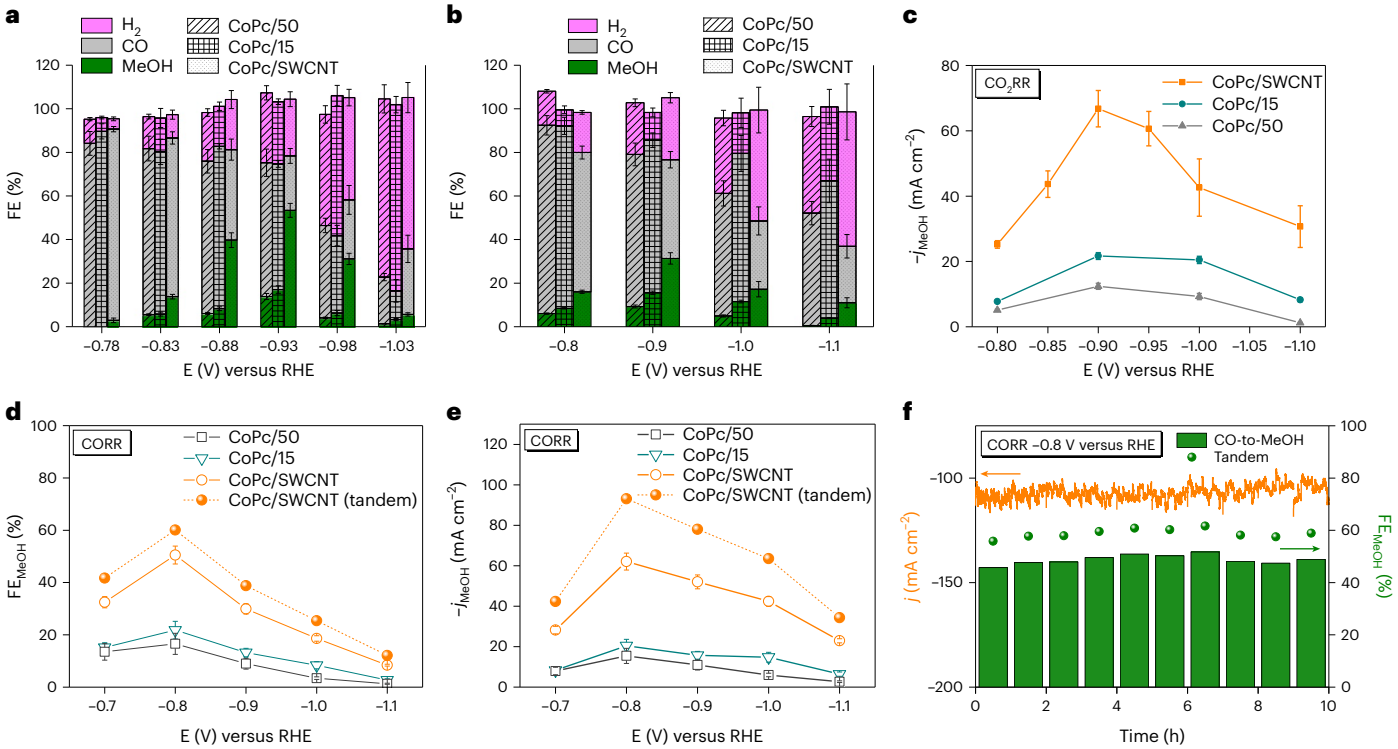

Fig. 3 | Electrochemical CO_2 reduction performance. a,**b**, FE of methanol, CO and H_2 in an H-cell with 0.5 M $KHCO_3$ as electrolyte (**a**) and in a flow cell with 0.1 M KOH + 3 M KCl as electrolyte (**b**). **c**, j_{MeOH} of CoPc/SWCNT, CoPc/15 and CoPc/50 catalysts in a flow cell under CO_2 atmosphere. **d**,**e**, FE_{MeOH} (**d**) and j_{MeOH} (**e**) of CoPc/SWCNTs, CoPc/15 and CoPc/50 in a flow cell under CO atmosphere. **f**, Long-term stability and corresponding FE_{MeOH} of CoPc/SWCNTs at −0.8 V versus RHE. The error bars indicate the s.d. among values from three repeated measurements.

provide ample surface area for coordinating CoPc. We then placed a flat CoPc catalyst within the van der Waals distance of the outside of the SWCNT. With the hydrogen atoms of the SWCNT frozen, we optimized the geometry of the CoPc when near the outside of the SWCNT wall. The MD simulation shows that the CoPc curves around the $C_{116}H_{28}$ such that the curvature of the catalyst and the CNT are equal. Additionally, the curved plane of the catalyst lies ~3.11 Å from the wall of the SWCNT, indicating strong π–π stacking between the catalyst and the SWCNT. Fixing the peripheral hydrogen of CoPc to maintain the pristine CoPc structure, however, results in a longer Co–$C_{116}H_{28}$ distance, which suggests a weaker Co–CNT interaction. We also explored how CoPc interacts with a large, flat sheet of carbon, which represents a MWCNT. In this case, the CoPc plane remained parallel to the flat $C_{116}H_{28}$ sheet with the distance between the two planes being ~3.37 Å. When we instead used 2D periodic graphene, the interplane distance is still predicted to be 3.37 Å. Thus, we conclude that the flat or curved $C_{116}H_{28}$ sheet properly mimics the graphene or SWCNT. The predicted structures from our MD calculations agree well with our quantum mechanical calculations and with our experimental spectroscopic data for curved and flat CoPc structures as shown in Fig. 2e,f and Supplementary Table 1. Moreover, DFT at the PBE-D3 level of theory predicts flat CoPc to reside 3.39 Å from graphene, in excellent agreement with the prediction. This justifies our claim that PQEq + UNB accurately captures non-bond geometries.

In addition to the geometric distortion of CoPc upon binding to the SWCNTs, we observe a shift in the N 1*s* indicating electronic structure distortion. DFT predicts four degenerate N 1*s* orbitals at −381.16 eV below the vacuum energy. Forcing the complex into the curved geometry breaks the degeneracy of the N 1*s* orbitals. Specifically, the four orbitals now range from −381.44 eV to −381.36 eV (0.08 eV variation). The N 1*s* orbitals are also stabilized in the curved complex by an average of −0.24 eV, indicating increased binding energy as observed in experiment (Fig. 2b).

Reaction energies predicted by grand canonical DFT

The different CO_2RR selectivity of curved and flat CoPc hints a change in the CO absorption step. To explore this, we applied grand canonical DFT to examine the energetics as a function of chemical potential. Our grand canonical potential kinetics (GCPK) method[36] keeps the applied potential constant for the initial and product states of each reaction step, just as in experiment (see Methods for more details). For CoPc on the SWCNTs, we use the curved CoPc generated from the MD simulation as the starting point. For CoPc on the MWCNTs, we start with the typical CoPc catalyst with D_{4h} symmetry. Liao and co-workers[37] recently suggested that at −1.0 V versus RHE (−1.4 V versus SHE at pH 6.8), the CoPc catalyst is spontaneously reduced to $CoPcH_4$ in water. Specifically, the four outward nitrogens of the Pc ligand are hydrogenated (hence PcH_4) with a free energy change of −2.92 eV relative to CoPc at 298.15 K. Thus, for our calculations we hydrogenate the four outward nitrogens of the Pc ligand for both curved and flat $CoPcH_4$. These hydrogenations are not likely to cause cobalt demetallization since the reductions do not occur at the Co–N sites.

The CO absorption energy as a function of applied potential is shown in Fig. 4a,b. We see that for the calculated potential window, the curved CoPc has stronger CO binding than the flat CoPc. At −1.0 V versus RHE, the curved $CoPcH_4$ binds CO by −1.41 eV and the flat $CoPcH_4$ binds CO by 0.25 eV. Thus, for flat $CoPcH_4$, CO production leads to immediate CO desorption, making further steps to methanol unlikely. For curved $CoPcH_4$, the CO remains bound to the catalyst, enabling further transformation to methanol; this agrees with the experiment, in which curved CoPc is selective towards methanol whereas flat CoPc is selective towards CO.

In Fig. 4c, the curved $CoPcH_4$ is higher in energy than the flat analogue due to the induced strain. However, the curved $CoPcH_4$(CO) is lower in energy than the flat analogue, because the strain makes for favourable CO binding. These two factors lead towards improved

https://doi.org/10.1038/s41929-023-01005-3

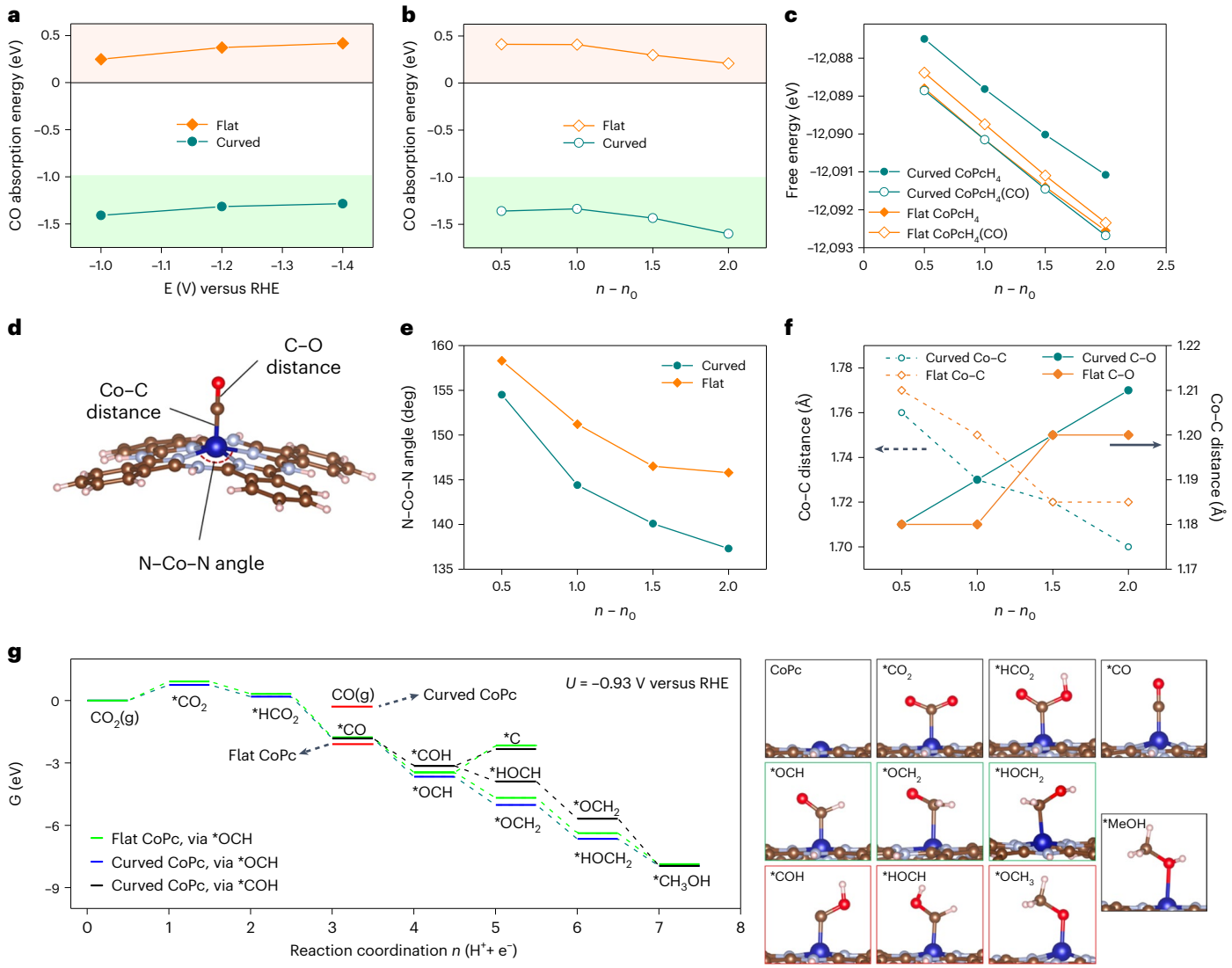

Fig. 4 | Mechanistic insight from quantum mechanics calculations. **a**,**b**, Absorption energy versus potential (U_{RHE}, V) (**a**) and $n - n_0$ (**b**), where n is the number of electrons added ($n - n_o = 1$ indicates 1 electron has been added to the neutral system). **c**, Free energies of curved and flat $CoPcH_4$ with and without CO adsorption versus $n - n_0$. **d**, Representative N–Co–N angle and Co–C and C–O distances of $CoPcH_4$. **e**, N–Co–N angle (degrees) versus $n - n_0$ for the curved and flat structures. **f**, Co–C and C–O distances (Å) versus $n - n_0$. **g**, Free energies (eV) at $U = -0.93$ V versus RHE and pH 7 for CO_2 reduction to methanol on curved and flat CoPc. ΔG_C and ΔG_F are reaction step free energies for the curved and flat CoPc, respectively. For flat CoPc it is favourable for CO to desorb so it is not available for subsequent steps toward methanol. For curved CoPc, it is not favourable to desorb CO, making it available for production of methanol. Green boxes indicate the preferred intermediates and red boxes indicate the higher-energy intermediates.

CO binding for curved CoPc, which ultimately improves methanol selectivity.

The distortion of the square pyramidal $CoPcH_4(CO)$ geometry on the SWCNTs is probably due to strong spin–orbit coupling in the d^7 configuration[38]. The four-coordinate planar Co(II) ion has degenerate d_{xz} and d_{yz} orbitals which lie below the singly occupied d_{xy}. Upon binding to the SWCNT, the cobalt distorts out of the nitrogen basal plane, swapping the d_{xz} and d_{yz} orbitals with the d_{xy} orbital, so that d_{xy} becomes doubly occupied lying below the doubly occupied d_{xz} and singly occupied d_{yz}.

We evaluated the geometries of the curved and flat $CoPcH_4(CO)$ intermediates at varying charge to understand how CO binding affinity changes with potential. We investigated the N–Co–N angle, the Co–C distance and the C–O distance (Fig. 4d). At all charges, the curved $CoPcH_4(CO)$ maintains a smaller N–Co–N angle than the flat analogue, indicating more out-of-plane distortion (Fig. 4e). For both cases, the angle decreases as additional electrons are introduced (potential becomes more negative). This is probably because electrons are occupying the d_{yz} orbital, and to minimize overlap with the in-plane p orbitals of the ligand, the cobalt distorts axially out of plane. The curved $CoPcH_4(CO)$ maintains a shorter Co–C distance for all charges until $n - n_0 = 1.5$, where the Co–C distance is 1.72 Å for both flat and curved cases (Fig. 4f). As electrons are added, the Co–C distance decreases, indicating stronger binding of cobalt to carbon. In this potential range, the first orbitals filled are d_{yz} and d_{z^2}, both of which can participate in bonding to CO. Because cobalt is more distorted in the curved case, these d orbitals are more easily occupied due to decreased overlap with the PcH_4 in-plane p orbitals, leading to more facile binding to CO. The curved $CoPcH_4(CO)$ maintains a longer C–O distance for all charges except for $n - n_0 = 1.5$, where the C–O distance is 1.20 Å for both the curved and flat $CoPcH_4(CO)$. As bonding between cobalt and carbon increases, the C=O bond becomes activated, increasing the bond distance. We consider this C=O bond activation desirable because it makes it easier to reduce CO, increasing selectivity towards methanol. Because

https://doi.org/10.1038/s41929-023-01005-3

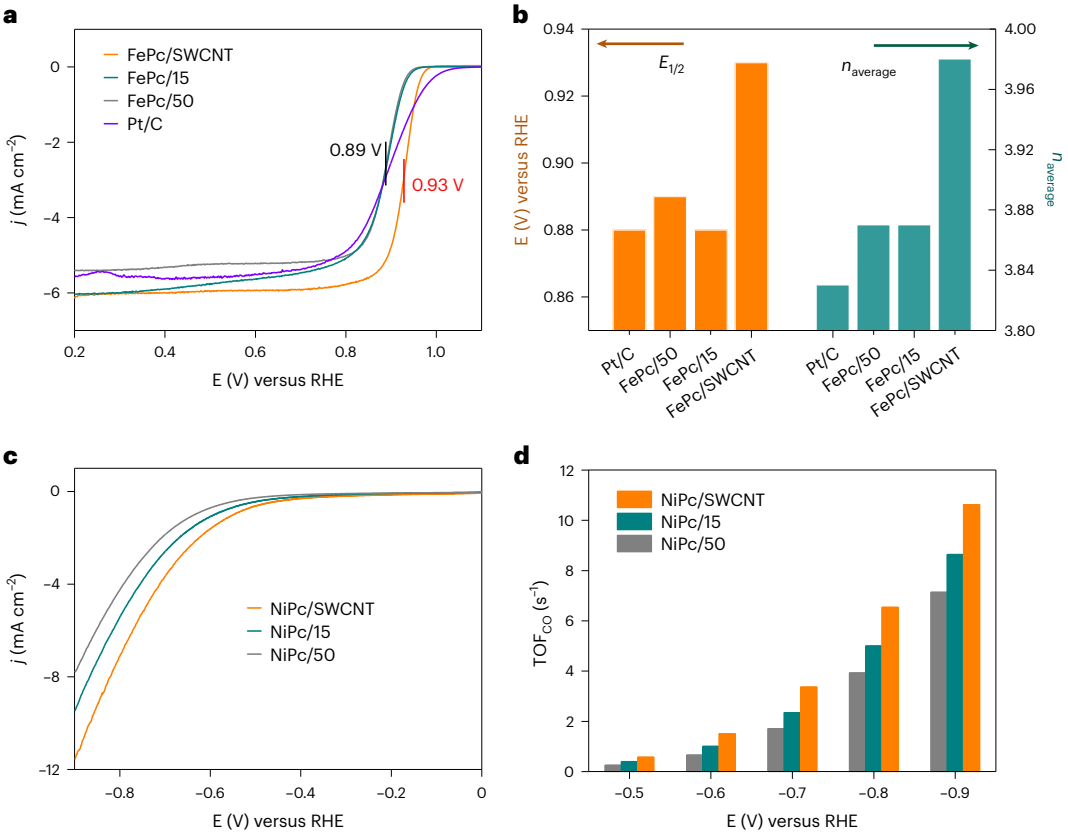

Fig. 5 | Support effect on other molecules. a,**b**, ORR LSV curves (**a**) and comparison of half-wave potentials and average electron transfer number (**b**) of FePc/SWCNT, FePc/15, FePc/50 and commercial Pt/C catalysts in O_2-saturated 0.1 M KOH electrolyte. **c**,**d**, CO_2RR LSV curves (**c**) and TOF_{CO} values (**d**) of NiPc/SWCNT, NiPc/15 and NiPc/50 in CO_2-saturated 0.5 M $KHCO_3$ electrolyte using an H-cell.

the C–O distance is longer in the curved $CoPcH_4(CO)$, CO reduction and further conversion to methanol will be more facile.

We explored the entire mechanism for the reduction of CO_2 to methanol on the curved and flat CoPc molecules using grand canonical DFT (Fig. 4g and Supplementary Fig. 31). The conditions of $U = -0.93$ V versus RHE and pH 7 were chosen to match that of experiment. The reduction of CO_2 to CO is straightforward: CO_2 binds to cobalt to form bent $*CO_2$, which is then reduced to form *HOCO. *HOCO undergoes an additional reduction at the protonated oxygen to liberate a H_2O and form *CO. At this point, for the flat CoPc, it is favourable for CO to desorb, and therefore subsequent steps to form $OHCH_3$ are not relevant. However, *CO is much more strongly bonding to SWCNTs, favouring reduction at carbon to form *OCH or at oxyegn to form *COH. For the curved and flat CoPc, we find *OCH to be more stable at −0.93 V versus RHE. Reduction of *OCH can lead to either $*OCH_2$ (reduction at carbon) or *HOCH (reduction at oxygen), while reduction of *COH leads to *HOCH. DFT predicts $*OCH_2$ to be more stable than *HOCH. At −0.93 V versus RHE, the oxygen of $*OCH_2$ carries negative charge, which permits carbon to make a covalent bond to cobalt; this ultimately keeps $*OCH_2$ from desorbing to form formaldehyde. From $*OCH_2$, the next reduction can yield either $*HOCH_2$ or $*OCH_3$. At −0.93 V versus RHE, $*HOCH_2$ is more stable. The final reduction yields methanol (*MeOH), which can be formed from $*HOCH_2$ or $*OCH_3$. The overall reduction of CO_2 to *MeOH is −7.97 for the curved CoPc, with the highest-energy intermediate being $*CO_2$. The most important reaction step for CO versus methanol formation is reduction of *CO to *OCH. We see that for the curved CoPc, this step is −1.84 eV. We note that methane is often competitive with methanol formation during CO_2RR. However, the methane mechanism usually requires multisite catalysts such that intermediates such as *C can coordinate to multiple catalyst centres[39,40]. Because CoPc is a single-site catalyst, *C would be severely undercoordinated, resulting in a high energy. Similarly, C_{2+} products also require multisite catalysts[39,40], and we do not observe them experimentally. Calculations on methane-forming pathways can be found in Supplementary Note 3.

In situ attenuated total reflectance-surface enhanced infrared absorption spectroscopy (ATR-SEIRAS; no resistance compensation) was performed to further characterize the reaction intermediates (Supplementary Fig. 32). For CoPc/SWCNTs, we found a C–H stretching mode at ~3,010 cm^{-1}, which could be from $*OCH_2$ or $*HOCH_2$. We also observe the aldehyde C–H stretch at ~2,765 cm^{-1}, which emerges at approximately −0.7 V and becomes stronger at higher overpotentials. For CoPc/50, we do not detect obvious signals between 2,600 and 3,200 cm^{-1}, probably because the poor *CO absorption prohibits subsequent reduction beyond *CO. A previous study showed that formaldehyde is a possible intermediate in methanol formation, based on the observation of a methanol signal from formaldehyde reduction[11]. Our ART-SEIRAS experiments supplemented with theoretical calculations explicitly confirm the $*OCH_2$ pathway for methanol production, in which the curved CoPc induced by SWCNTs plays an indispensable role.

SWCNT-induced distortion of other molecular catalysts

We extended the concept of CNT-induced molecular distortion to enhance the catalytic performance of other molecular systems. We investigated the oxygen reduction activity of FePc/SWCNTs in O_2-saturated 0.1 M KOH via measurements on a rotating disk electrode (RDE). Linear sweep voltammetry (LSV, Fig. 5a) indicates that FePc/SWCNTs achieve higher activity than FePc/MWCNTs, with a more positive onset (E_{onset}) and half-wave potential ($E_{1/2}$) than all other samples. The $E_{1/2}$ of FePc/SWCNTs is 0.93 V, which is 40 mV more positive than

those of FePc/15, FePc/50 and Pt/C. We calculated the average electron transfer number (n) from the LSV curves with different rotation rates using Koutecky–Levich (K-L) plots (Supplementary Fig. 33)[41]. We find n = 3.98 for FePc/SWCNTs, close to the theoretical limit of 4.00 for a four-electron reduction process. In comparison, FePc/15 and FePc/50 show n = 3.87, indicating that curved FePc performs ORR more rapidly (Fig. 5b).

We also measured the CO_2RR performance of NiPc with three different diameter CNTs in an H-cell containing CO_2-saturated 0.5 M $KHCO_3$. All samples lead only to gas products with similar FE_{CO} (Supplementary Fig. 34). However, as shown in Fig. 5c,d, the NiPc/SWCNTs show higher current density and CO turnover frequency (TOF_{CO}) in CO_2RR performance than NiPc/15 and NiPc/50.

Conclusions

CNTs have been widely used as supports to prevent sintering and agglomeration of nanoparticles, and as conductive substrates for electrochemical applications. Our work shows a role of CNTs for inducing ångström-scale molecular distortions to tailor catalytic activity. Using CoPc monodispersed on CNTs, we demonstrated the benefit of geometrically distorted CoPc on electrocatalysis, confirmed by various spectroscopic data, MD simulations and DFT calculations. We show that for the CO_2RR, CoPc/SWCNTs can achieve 53.4% FE_{MeOH} with excellent durability, which is dramatically improved over conventional CoPc/MWCNTs. In a flow cell configuration, we achieved a j_{MeOH} of 66.8 mA cm^{-2} with an FE_{MeOH} of 31.3% in a CO_2 atmosphere and a j_{MeOH} of 62.1 mA cm^{-2} with an FE_{MeOH} of 50.5% in a CO atmosphere. We reach a total FE_{MeOH} of 60.0% with the CO_2RR–CORR tandem reaction. Our MD and DFT studies find that this performance is enabled by the strong CO adsorption on CoPc/SWCNT, which facilitates production of methanol instead of CO. These results explain why CO is the prevailing product in most CoPc literature, where the substrates are often wide CNTs or graphitic carbon. We also show the different activities of ORR for FePc and CO_2RR for NiPc, which change with CNT support. Our study may prompt future investigation of curvature-dependent reactivity for other molecular catalysts at the nanometre scale.

Methods

Preparation of CoPc/SWCNT catalysts

All CNTs were bought from XFNANO; SWCNTs (synthesized by a floating catalyst chemical vapour deposition method and containing both semiconducting and metallic elements) were pretreated in 6 mol l^{-1} HCl solution for 12 h to remove any metal impurities. After that, the SWCNT sample was filtered, washed with deionized water and freeze-dried. Then, 20 mg of the purified SWCNTs was subsequently dispersed in 20 ml of dimethylformamide (DMF) using sonication. Then, an appropriate amount of cobalt(II) phthalocyanine (J&K Scientific) dissolved in 5 ml DMF was added to the SWCNT suspension. The mixture was sonicated for 30 min to obtain a well-mixed suspension, which was further stirred at room temperature for 24 h. Subsequently, the mixture was centrifuged, and the precipitate was washed with DMF, ethanol and deionized water. Finally, the precipitate was lyophilized to yield the final product. The samples with CNT substrates of different-diameter SWCNTs, that is, 4–6 nm, 5–15 nm, 10–20 nm, 20–30 nm and >50 nm, were denoted as CoPc/SWCNTs, CoPc/5, CoPc/10, CoPc/15, CoPc/25 and CoPc/50, respectively. The CoPc/SWCNT-M and CoPc/SWCNT-S were prepared with pure metallic and semiconductor SWCNTs (XFN13-2 and XFN08-2) as the substrates, respectively. The f-CoPc-SWCNTs were synthesized through a modified covalent strategy[42]. The weight percentages of metal in all MPc/CNT composites are ~0.22% determined by inductively coupled plasma optical emission spectroscopy.

Preparation of FePc/SWCNT and NiPc/SWCNT catalysts

The preparation process of FePc/SWCNTs and NiPc/SWCNTs is same as above, except that CoPc is replaced by FePc and NiPc. The samples with different CNT diameter substrates of 10–20 and >50 nm were denoted as FePc/15, FePc/50, NiPc/15 and NiPc/50, respectively.

Materials characterization

The morphology of samples was characterized using transmission electron microscopy (TEM; Philips Technai 12) equipped to perform energy-dispersive X-ray spectroscopy. Inductively coupled plasma optical emission spectroscopy measurements were conducted on Optima 8000 spectrometer. Samples were digested in hot concentrated HNO_3 for 1 h and diluted to the desired concentrations. Ultraviolet–visible spectroscopy was performed on a Shimadzu 1700 spectrophotometer in ethanol solution with a concentration of 1×10^{-5} mol ml^{-1}. The XPS data were collected on a Thermo ESCALAB 250Xi spectrometer equipped with a monochromatic Al K radiation source (1,486.6 eV; pass energy, 20.0 eV). The data were calibrated with C 1*s* 284.6 eV. Raman spectra were collected using a LabRAM HR800 laser confocal micro-Raman spectrometer with a laser wavelength of 514.5 nm. STEM was performed on a double spherical-aberration-corrected FEI Themis Z microscope at 60 kV.

XAFS measurements were performed in fluorescence mode using a Lytle detector at beamline 01C1 of the National Synchrotron Radiation Research Center (NSRRC), Taiwan. The electron storage ring was operated at 1.5 GeV with a constant current of ~360 mA. A Si(111) double-crystal monochromator was used to scan the photon energy. XANES analyses were conducted using Athena software based on the IFEFFIT program[43] to determine the structural environment of cobalt atoms. The averaged X-ray absorption spectra were first normalized to the absorption edge height, and the background was removed using the automatic background subtraction routine AUTOBK implemented in the Athena software[44]. A reference foil of cobalt was used for energy calibration of the monochromator, which was applied to all spectra. The Co K-edge calibration was set to the first inflection point of the reference foil, set at 7,709 eV for easy comparison with other work[45]. Quantitative information on the radial distribution of neighbouring atoms surrounding the cobalt atoms was derived from the EXAFS data. An established data-reduction method was used to extract the EXAFS χ functions from the raw experimental data using the IFEFFIT software.

Electrochemical measurements

The H-cell catalyst ink was prepared by dispersing 2 mg of catalyst in 1 ml of ethanol with 20 µl 5 wt% Nafion solution (Nafion 117; Sigma Aldrich) and sonicated for 1 h. Then 200 µl of the ink was drop-cast on the glassy carbon working electrode and subsequently dried naturally. The loading was 0.4 mg cm^{-2}. The electrochemical performance was carried out in a customized glass H-cell. Platinum and Ag/AgCl were used as the counterelectrode and reference electrodes, respectively. The working electrode was separated from the counterelectrode by the Nafion 117 membrane (Fuel Cell Store). Before use, the Ag/AgCl reference was calibrated as reported previously[46,47]. All potentials in this study were converted to the reversible hydrogen electrode (RHE) according to the Nernst equation (E (versus RHE) = E (versus Ag/AgCl) + 0.231 + 0.0592 × pH). Then 10 ml of 0.5 M $KHCO_3$ solution electrolyte was added into both the working compartment and the countercompartment. The cell was purged with high-purity CO_2 gas (Linde, 99.999%, 20 sccm) for 30 min prior to all electrochemical measurements. The electrochemical measurements were controlled and recorded with a CHI 650E potentiostat. Automatic iR (85%) compensation was used. Gas-phase products were quantified by an online gas chromatograph (Ruimin GC 2060) equipped with a methanizer, a Hayesep-D capillary column, a flame ionization detector for CO, and a thermal conductivity detector for H_2. The CO_2 flow rate was controlled at 3 sccm using a standard series mass flow controller (Alicat Scientific mc-50 sccm). The liquid products were quantified after electrocatalysis using ^{1}H NMR spectroscopy with solvent (H_2O) suppression by mixing 450 µl of electrolyte with 50 µl of a solution of 10 mM dimethylsulfoxide in D_2O as internal standards for the ^{1}H NMR analysis. The concentration

of methanol was calculated using the ratio of the area of the methanol peak (at a chemical shift of 3.32 ppm) to that of the dimethylsulfoxide internal standard. Electrolytes containing $^{13}CO_2$ in 0.5 M $KH^{13}CO_3$ were prepared by bubbling $^{13}CO_2$ into 0.5 M KOH for more than 30 min.

For CO_2RR flow electrolysis, to get a good FE_{MeOH} in the flow cell, CoPc/SWCNTs with high-CoPc-loading catalysts were prepared using a chemical vapour deposition-type procedure according to our previous work[24]. Then, 5 mg of catalyst mixed with 40 µl Nafion solution was deposited in 2 ml ethanol, sonicated for 1 h to form a uniform ink and drop-cast on a 1 × 2.5 cm^2 gas diffusion layer (Sigracet-28BC) (mass loading of the sample, 1 mg cm^{-2}). Platinum and Ag/AgCl were used as the counterelectrode and the reference electrode, respectively. The cathode chamber and anode chamber were separated by Nafion 117 membrane (Fuel Cell Store). The CO_2 gas flow (flow rate, 10 sccm) was applied to the cathode side, while 0.1 M KOH + 3 M KCl and 1 M KOH electrolyte at a flow rate of 5 ml min^{-1} was circulated in the cathode and anode chamber, respectively. The cathode electrolyte was collected in a flask with an ice bath for NMR testing.

For CORR flow electrolysis, the working-electrode preparation process and cell device are the same as the CO_2RR flow cell, except that the feed gas is changed to CO.

For FePc/CNT ORR measurement, 2 mg of catalyst was dispersed in 1 ml of solution containing 0.882 ml of ethanol, 0.098 ml of water and 20 µl of 5 wt% Nafion solution, which was sonicated for 1 h to form a homogeneous catalyst ink. All the catalysts were cast onto the RDE (diameter, 5 mm) with a loading amount of 0.2 mg cm^{-2}.

RDE tests were performed in O_2-saturated 0.1 mol l^{-1} KOH solution with a scan rate of 10 mV s^{-1} between 1.1 V and 0.2 V at different rotating rates using a PINE 636 RDE system and a CHI650 workstation. Ag/AgCl and platinum were used as the reference electrode and the counterelectrode, respectively. All potentials were converted to the RHE.

The electron transfer number (n) was determined by the Koutecky–Levich equations:

$$\frac{1}{J} = \frac{1}{J_L} + \frac{1}{J_K} = \frac{1}{B\omega^{\frac{1}{2}}} + \frac{1}{J_K} \quad (1)$$

$$B = 0.62nFC_0D_0^{\frac{2}{3}}V^{-\frac{1}{6}} \quad (2)$$

where J is the measured current density, J_K and J_L are the kinetic and limiting current densities, ω is the angular velocity of the disk, n is the overall number of electrons transferred in oxygen reduction, F is the Faraday constant (96,485 C mol^{-1}), C_0 is the bulk concentration of O_2 (1.2×10^{-6} mol cm^{-3}), D_0 is the diffusion coefficient of O_2 in 0.1 M KOH (1.9×10^{-5} cm^2 s^{-1}) and V is the kinematic viscosity of the electrolyte (0.01 cm^2 s^{-1}).

For NiPc/CNT CO_2RR measurement, 2 mg of catalyst was mixed in 1 ml of ethanol with 20 µl 5 wt% Nafion solution and sonicated for 1 h to form a homogeneous catalyst ink. All the catalysts were drop-cast onto carbon paper (Toray TGP-H-060; Fuel Cell Store) (diameter, 0.5 inch) with a 0.4 mg cm^{-2} loading. The electrochemical performance was measured in a customized three-compartment cell, as previously reported[16,42]. A platinum foil and Ag/AgCl leak-free reference (LF-2; Innovative Instrument) were used as the counterelectrode and the reference electrode, respectively. The working electrode was separated from the counterelectrode by the Nafion 117 membrane. The electrolyte was 0.5 M $KHCO_3$.

In situ ATR-SEIRAS was measured with a PerkinElmer Spectrum 100 spectrometer equipped with a mercury cadmium telluride detector, a variable-angle specular reflectance accessory (Veemax III; Pike Technologies), and a one-compartment cell (LingLu Instruments) including a platinum counterelectrode, an Ag/ AgCl reference electrode, a gas inlet port and a gas outlet port. A catalyst-coated silicon ATR crystal with gold film underlayer is placed in the cell as the working electrode. Before electrochemical measurements, the electrolyte (0.5 M $KHCO_3$ saturated with CO_2) was injected into the cell and purged with high-purity CO_2 (99.999%) for 15 min. A CHI1242C potentiostat was employed to record the electrochemical response. The spectrum was collected stepwise from −0.2 V to −1.1 V versus RHE with a dwell time of 3 min at each potential.

Computational methods

The atomic coordinates of optimized models are provided in Supplementary Data 1. Molecular dynamics simulations were performed using the LAMMPS software[48]. For these simulations we used the UFF for valence interactions (bond, angle and dihedral terms) combined with the RexPoN[49] UNB potentials to describe van der Waals interactions, and the PQEq scheme for electrostatics. To represent the nanotube surface, we used a $C_{116}H_{28}$ sheet. To mimic a MWCNT, we used flat $C_{116}H_{28}$. To mimic the SWCNT, the $C_{116}H_{28}$ was bent to match the curvature of a 2-nm-diameter SWCNT. To maintain the overall curvature of the graphitic sheet, the edge hydrogens were fixed. To minimize the CNT–CoPc systems we used conjugate gradients followed by the steepest descent.

DFT geometry optimizations were performed using VASP 5.4.4[50] with the solvation module[51]. For the curved species, the edge hydrogen atoms of the Pc ligand were fixed to maintain the curvature. Spin polarization was allowed during optimization. We used the PBE[52] functional with the D3[53] empirical correction for London dispersion forces. The kinetic energy cutoff was set to 500 eV, the wavefunction cutoff was set to 1×10^{-5} eV, and the force cutoff was set to 0.03 eV $Å^{-1}$. All VASP optimizations were in a 20 $Å^3$ box with a $1 \times 1 \times 1$ k-point Monkhorst–Pack grid.

To obtain the energy as a function of applied potential, we performed single point energy calculations using JDFTx[54] with the CANDLE[55] solvation model. Because our systems are finite (non-periodic), we were able to perform vibrational frequency calculations using Jaguar v.10.9 (ref. 56) to obtain mode-dependent entropies, zero-point energies and enthalpies at 298.15 K.

In the GCP method, we first calculate the free energy (F) as a function of the number of electrons (n). $F(n)$ includes the librational and vibrational contributions to the zero-point energy, entropy and enthalpy at 298.15 K. $F(n)$ has a quadratic form, which we write as equation (3):

$$F(n) = a(n - n_0)^2 + b(n - n_0) + c \quad (3)$$

where the a, b and c parameters are fitted to the quantum mechanical calculations. Here a should be positive to obtain a stable system (minima as opposed to maxima at $n = n_0$) and n_0 is the number of explicit electrons for a neutral system (explicit because we utilize pseudopotentials). The quadratic form of $F(n)$ is strictly verified in our calculations.

Then we use the Legendre transformation on $F(n)$ to obtain equation (4):

$$G(n;U) = F(n) - ne(U_{SHE} - U) \quad (4)$$

We then minimize G with respect to U with a simple derivative:

$$\frac{dG(n;U)}{dn} = 0 \text{ or } \mu_e = e(U_{SHE} - U) = \frac{dF(n)}{dn} \quad (5)$$

This leads to

$$\begin{aligned} GCP(U) &= \min G(n;U) = \min(F(n) - ne(U_{SHE} - U)) \\ &= -\frac{1}{4a}(b - \mu_{e,SHE} + eU)^2 + c - n_0\mu_{e,SHE} + n_0eU \end{aligned} \quad (6)$$

which can be written as

$$GCP(U) = -\frac{C_{diff}}{2}(U - U_{PZC})^2 + n_0eU + F_0 - n_0\mu_{e,SHE} \quad (7)$$

where C_{diff} is the differential capacitance and U_{PZC} is the value of U at the point of zero charge. When the GCP is at its minimum, there is an inverse

relationship between n and the applied potential (C_{diff} has a positive value), meaning adding electrons makes the applied potential more negative. The GCP method assumes a metallic system. However, our CoPc systems have finite HOMO–LUMO gaps because the conductive CNTs are not explicitly included. We have done previous GCP with a similar inconsistency and found excellent agreement between the predicted and experimental onset potentials and current versus applied potential, validating the use of GCP for finite-gap systems deposited on conducting supports[57].

Although *H is also competing[58,59], it is not pertinent to our main result. Indeed, we found that *H adsorption does not change substantially under different potentials (Supplementary Fig. 35).

Data availability

All data are available from the authors upon reasonable request.

References

1. Yang, S. et al. Tuning the optical, magnetic, and electrical properties of $ReSe_2$ by nanoscale strain engineering. *Nano Lett.* **15**, 1660–1666 (2015).
2. Levy, N. et al. Strain-induced pseudo–magnetic fields greater than 300 tesla in graphene nanobubbles. *Science* **329**, 544–547 (2010).
3. Zeng, M. et al. Bandgap tuning of two-dimensional materials by sphere diameter engineering. *Nat. Mater.* **19**, 528–533 (2020).
4. Li, H. et al. Activating and optimizing MoS_2 basal planes for hydrogen evolution through the formation of strained sulphur vacancies. *Nat. Mater.* **15**, 48–53 (2016).
5. Nam, D. H. et al. Molecular enhancement of heterogeneous CO_2 reduction. *Nat. Mater.* **19**, 266–276 (2020).
6. Navarro-Jaén, S. et al. Highlights and challenges in the selective reduction of carbon dioxide to methanol. *Nat. Rev. Chem.* **5**, 564–579 (2021).
7. Boutin, E. & Robert, M. Molecular electrochemical reduction of CO_2 beyond two electrons. *Trends Chem.* **3**, 359–372 (2021).
8. Kapusta, S. & Hackerman, N. Carbon dioxide reduction at a metal phthalocyanine catalyzed carbon electrode. *J. Electrochem. Soc.* **131**, 1511–1514 (1984).
9. Wu, Y., Jiang, Z., Lu, X., Liang, Y. & Wang, H. Domino electroreduction of CO_2 to methanol on a molecular catalyst. *Nature* **575**, 639–642 (2019).
10. Wu, Y., Liang, Y. & Wang, H. Heterogeneous molecular catalysts of metal phthalocyanines for electrochemical CO_2 reduction reactions. *Acc. Chem. Res.* **54**, 3149–3159 (2021).
11. Boutin, E. et al. Aqueous electrochemical reduction of carbon dioxide and carbon monoxide into methanol with cobalt phthalocyanine. *Angew. Chem. Int. Ed.* **58**, 16172–16176 (2019).
12. Chang, Q. et al. Metal-coordinated phthalocyanines as platform molecules for understanding isolated metal sites in the electrochemical reduction of CO_2. *J. Am. Chem. Soc.* **144**, 16131–16138 (2022).
13. Zhang, X. et al. Highly selective and active CO_2 reduction electrocatalysts based on cobalt phthalocyanine/carbon nanotube hybrid structures. *Nat. Commun.* **8**, 14675 (2017).
14. Han, N. et al. Supported cobalt polyphthalocyanine for high-performance electrocatalytic CO_2 reduction. *Chem* **3**, 652–664 (2017).
15. Zhu, M., Ye, R., Jin, K., Lazouski, N. & Manthiram, K. Elucidating the reactivity and mechanism of CO_2 electroreduction at highly dispersed cobalt phthalocyanine. *ACS Energy Lett.* **3**, 1381–1386 (2018).
16. Song, Y. et al. Zwitterionic ultrathin covalent organic polymers for high-performance electrocatalytic carbon dioxide reduction. *Appl. Catal. B* **284**, 119750 (2021).
17. Kobayashi, N., Fukuda, T., Ueno, K. & Ogino, H. Extremely non-planar phthalocyanines with saddle or helical conformation: synthesis and structural characterizations. *J. Am. Chem. Soc.* **123**, 10740–10741 (2001).
18. Fukuda, T., Homma, S. & Kobayashi, N. Deformed phthalocyanines: synthesis and characterization of zinc phthalocyanines bearing phenyl substituents at the 1-, 4-, 8-, 11-, 15-, 18-, 22-, and/or 25-positions. *Chem. Eur. J.* **11**, 5205–5216 (2005).
19. Alvarez, L. et al. One-dimensional molecular crystal of phthalocyanine confined into single-walled carbon nanotubes. *J. Phys. Chem. C* **119**, 5203–5210 (2015).
20. Liu, Z., Zhang, X., Zhang, Y. & Jiang, J. Theoretical investigation of the molecular, electronic structures and vibrational spectra of a series of first transition metal phthalocyanines. *Spectrochim. Acta A* **67**, 1232–1246 (2007).
21. Wang, X. H., Zheng, C. C. & Ning, J. Q. Influence of curvature strain and van der Waals force on the inter-layer vibration mode of WS_2 nanotubes: a confocal micro-Raman spectroscopic study. *Sci. Rep.* **6**, 6–11 (2016).
22. Zhang, J. et al. How to manipulate through-space conjugation and clusteroluminescence of simple AIEgens with isolated phenyl rings. *J. Am. Chem. Soc.* **143**, 9565–9574 (2021).
23. Krichevsky, D. M. et al. Magnetic nanoribbons with embedded cobalt grown inside single-walled carbon nanotubes. *Nanoscale* **14**, 1978–1989 (2022).
24. Tian, P. et al. Curvature-induced electronic tuning of molecular catalysts for CO_2 reduction. *Catal. Sci. Technol.* **11**, 2491–2496 (2021).
25. Papageorgiou, N. et al. Physics of ultra-thin phthalocyanine films on semiconductors. *Prog. Surf. Sci.* **77**, 139–170 (2004).
26. Palmgren, P. et al. Strong interactions in dye-sensitized interfaces. *J. Phys. Chem. C* **2**, 5972–5977 (2008).
27. Wu, X. et al. Molecularly dispersed cobalt phthalocyanine mediates selective and durable CO_2 reduction in a membrane flow cell. *Adv. Funct. Mater.* **32**, 2107301 (2022).
28. Pan, Y. et al. Design of single-atom Co-N5 catalytic site: a robust electrocatalyst for CO_2 reduction with nearly 100% CO selectivity and remarkable stability. *J. Am. Chem. Soc.* **140**, 4218–4221 (2018).
29. Han, G. et al. Substrate strain tunes operando geometric distortion and oxygen reduction activity of CuN_2C_2 single-atom sites. *Nat. Commun.* **12**, 6335 (2021).
30. Kuhl, K. P. et al. Electrocatalytic conversion of carbon dioxide to methane and methanol on transition metal surfaces. *J. Am. Chem. Soc.* **136**, 14107–14113 (2014).
31. Zhang, X. et al. Selective and high current CO_2 electro-reduction to multicarbon products in near-neutral KCl electrolytes. *J. Am. Chem. Soc.* **143**, 3245–3255 (2021).
32. Gu, J. et al. Modulating electric field distribution by alkali cations for CO_2 electroreduction in strongly acidic medium. *Nat. Catal.* **5**, 268–276 (2022).
33. Rappé, A. K., Casewit, C. J., Colwell, K. S., Goddard, W. A. & Skiff, W. M. UFF, a full periodic table force field for molecular mechanics and molecular dynamics simulations. *J. Am. Chem. Soc.* **114**, 10024–10035 (1992).
34. Naserifar, S., Brooks, D. J., Goddard, W. A. & Cvicek, V. Polarizable charge equilibration model for predicting accurate electrostatic interactions in molecules and solids. *J. Chem. Phys.* **146**, 124117 (2017).
35. Naserifar, S. et al. Accurate non-bonded potentials based on periodic quantum mechanics calculations for use in molecular simulations of materials and systems. *J. Chem. Phys.* **151**, 154111 (2019).
36. Sundararaman, R., Goddard, W. A. & Arias, T. A. Grand canonical electronic density-functional theory: algorithms and applications to electrochemistry. *J. Chem. Phys.* **146**, 114104 (2017).
37. Shi, L. L., Li, M., You, B. & Liao, R. Z. Theoretical study on the electro-reduction of carbon dioxide to methanol catalyzed by cobalt phthalocyanine. *Inorg. Chem.* **61**, 16549–16564 (2022).

38. Jurca, T. et al. Single-molecule magnet behavior with a single metal center enhanced through peripheral ligand modifications. *J. Am. Chem. Soc.* **133**, 15814–15817 (2011).
39. Birdja, Y. Y. et al. Advances and challenges in understanding the electrocatalytic conversion of carbon dioxide to fuels. *Nat. Energy* **4**, 732–745 (2019).
40. Nitopi, S. et al. Progress and perspectives of electrochemical CO_2 reduction on copper in aqueous electrolyte. *Chem. Rev.* **119**, 7610–7672 (2019).
41. Chen, K. et al. Iron phthalocyanine with coordination induced electronic localization to boost oxygen reduction reaction. *Nat. Commun.* **11**, 4173 (2020).
42. Su, J. et al. Building a stable cationic molecule/electrode interface for highly efficient and durable CO_2 reduction at an industrially relevant current. *Energy Environ. Sci.* **14**, 483–492 (2021).
43. Ravel, B. & Newville, M. ATHENA, ARTEMIS, HEPHAESTUS: data analysis for X-ray absorption spectroscopy using IFEFFIT. *J. Synchrotron Radiat.* **12**, 537–541 (2005).
44. Newville, M. IFEFFIT: interactive XAFS analysis and FEFF fitting. *J. Synchrotron Radiat.* **8**, 322–324 (2001).
45. Mathisen, K. et al. An in situ XAS study of the cobalt rhenium catalyst for ammonia synthesis. *Top. Catal.* **61**, 225–239 (2018).
46. Song, Y. et al. Atomically thin, ionic covalent organic nanosheets for stable, high-performance carbon dioxide electroreduction. *Adv. Mater.* **34**, 2110496 (2022).
47. Ye, R. et al. In situ formation of metal oxide nanocrystals embedded in laser-induced graphene. *ACS Nano* **9**, 9244–9251 (2015).
48. Thompson, A. P. et al. LAMMPS—a flexible simulation tool for particle-based materials modeling at the atomic, meso, and continuum scales. *Comput. Phys. Commun.* **271**, 108171 (2022).
49. Naserifar, S. & Goddard, W. A. The quantum mechanics-based polarizable force field for water simulations. *J. Chem. Phys.* **149**, 174502 (2018).
50. Allouche, A. Gabedit—a graphical user interface for computational chemistry softwares. *J. Comput. Chem.* **32**, 174–182 (2012).
51. Mathew, K., Sundararaman, R., Letchworth-Weaver, K., Arias, T. A. & Hennig, R. G. Implicit solvation model for density-functional study of nanocrystal surfaces and reaction pathways. *J. Chem. Phys.* **140**, 084106 (2014).
52. Perdew, J. P., Burke, K. & Ernzerhof, M. Generalized gradient approximation made simple. *Phys. Rev. Lett.* **77**, 3865–3868 (1996).
53. Grimme, S., Antony, J., Ehrlich, S. & Krieg, H. A consistent and accurate ab initio parametrization of density functional dispersion correction (DFT-D) for the 94 elements H–Pu. *J. Chem. Phys.* **132**, 154104 (2010).
54. Sundararaman, R. et al. JDFTx: software for joint density-functional theory. *SoftwareX* **6**, 278–284 (2017).
55. Sundararaman, R. & Goddard, W. A. The charge-asymmetric nonlocally determined local-electric (CANDLE) solvation model. *J. Chem. Phys.* **142**, 064107 (2015).
56. Bochevarov, A. D. et al. Jaguar: a high-performance quantum chemistry software program with strengths in life and materials sciences. *Int. J. Quantum Chem.* **113**, 2110–2142 (2013).
57. Song, J. et al. Reaction mechanism and strategy for optimizing the hydrogen evolution reaction on single-layer 1T′ WSe_2 and WTe_2 based on grand canonical potential kinetics. *ACS Appl. Mater. Interfaces* **13**, 55611–55620 (2021).
58. Bagger, A., Ju, W., Varela, A. S., Strasser, P. & Rossmeisl, J. Electrochemical CO_2 reduction: a classification problem. *ChemPhysChem* **18**, 3266–3273 (2017).
59. Bagger, A., Ju, W., Varela, A. S., Strasser, P. & Rossmeisl, J. Electrochemical CO_2 reduction: classifying Cu facets. *ACS Catal.* **9**, 7894–7899 (2019).

Acknowledgements

R.Y. acknowledges support from the Guangdong Basic and Applied Basic Research Fund (2022A1515011333), the Hong Kong Research Grant Council (21300620, 11307120, 11309723), the State Key Laboratory of Marine Pollution (SKLMP/IRF/0029) and the Shenzhen Science and Technology Program (JCYJ20220818101204009 and 2021Szvup129). C.B.M. and W.A.G. acknowledge support from the Liquid Sunlight Alliance, which is supported by the US Department of Energy, Office of Science, Office of Basic Energy Sciences, Fuels from Sunlight Hub under award number DE-SC0021266. B.Z.T. acknowledges support from the Shenzhen Key Laboratory of Functional Aggregate Materials (ZDSYS20211021111400001) and the Science Technology Innovation Commission of Shenzhen Municipality (KQTD20210811090142053, JCYJ20220818103007014). We thank W. Zhai and L. Wang for help with Raman characterization, and W. Li for his assistance with high-resolution TEM imaging.

Author contributions

R.Y. conceived and designed the research. R.Y., W.A.G. and B.Z.T. supervised the research. J.S. carried out most of the experiments and C.B.M. performed the calculations. Y.S., L.H., Y.L., G.L., Y.X., J.Z. and H.S. conducted part of the experiments. P.X., M.M.-J.L. and H.M.C. performed the X-ray absorption spectroscopy experiment and analysis. H.W. and M.Z. performed the in situ Fourier transform infrared studies. R.Y., W.A.G., J.S., C.B.M. and M.R. analysed the data and wrote the manuscript with input from the other authors.

Competing interests

The authors declare no competing interests.

Additional information

Supplementary information The online version contains supplementary material available at https://doi.org/10.1038/s41929-023-01005-3.

Correspondence and requests for materials should be addressed to William A. Goddard or Ruquan Ye.

Peer review information *Nature Catalysis* thanks Fuqiang Huang and the other, anonymous, reviewers for their contribution to the peer review of this work.